ACS Photonics

Open Access



pubs.acs.org/journal/apchd5

Article

# Vibrational Mode-Selective Infrared Spectroscopy at the Monolayer Level Using Silicon Quasi-Bound States in the Continuum

Keisuke Watanabe* and Tadaaki Nagao

Cite This: ACS Photonics 2025, 12, 6876−6883

Read Online

ACCESS | Metrics & More | Article Recommendations | Supporting Information

**ABSTRACT:** Surface-enhanced infrared absorption (SEIRA) boosts the sensitivity of infrared spectroscopy by leveraging the strong light−matter interactions induced by localized optical resonances in nanostructures. While most SEIRA studies have focused on metallic nanostructures, all-dielectric alternatives eliminate the unwanted optical ohmic losses as well as collisional damping of the plasma waves, potentially enabling higher-performance and lower-cost vibrational infrared spectroscopic platforms. In this study, we fabricate silicon-based all-dielectric metasurfaces that support quasi-bound states in the continuum (qBICs) and systematically investigate their SEIRA performance by varying the thickness of the spin-coated poly(methyl methacrylate) (PMMA) films, radiative quality factors, and spectral detuning. Furthermore, we quantify the enhancement factor (EF) for vibrational signals originating from the surface-adsorbed molecules, achieving a SEIRA enhancement factor exceeding $10^4$, which corresponds to the sensitivity at the monolayer level. Our findings provide practical design principles for metal-free, highly sensitive, and wavelength-selective infrared spectroscopy systems based on low-loss dielectric metasurfaces.

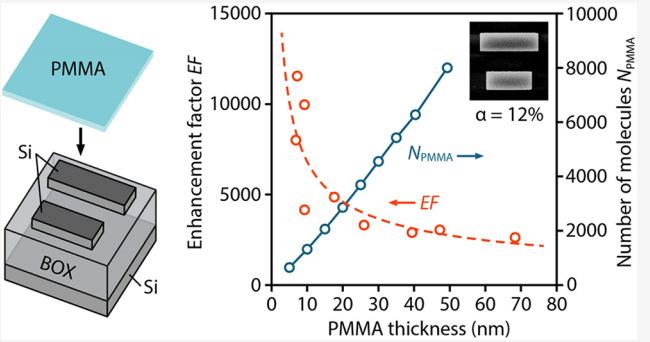


**KEYWORDS:** *metasurfaces, bound states in the continuum, silicon, all-dielectric, infrared spectroscopy*



## INTRODUCTION

Molecule-specific vibrations and phonons in the mid-infrared regime are fundamental to analytical chemistry[1] and are widely used to extract atom-scale structural information about molecules, including chemical bonds and configurations.[2] However, certain molecular vibrations exhibit intrinsically small absorption cross sections in infrared spectroscopy, posing significant challenges in detecting trace amounts of molecules. Similarly, the detection of thin-film adsorbates requires highly sensitive measurements to fully exploit the potential of infrared spectroscopy. Surface-enhanced infrared absorption (SEIRA)[3] and surface-enhanced Raman scattering (SERS)[4] are central techniques that significantly amplify the vibrational signals of analyte molecules, offering pathways toward ultrasensitive detection. Both these spectroscopic techniques rely on localized electric field enhancement in micro/nano resonators or optical nanoantennas.[5,6] However, conventionally employed metallic nanostructures[7−11] suffer from high optical ohmic losses and collisional damping of oscillating charge density waves, which limit the achievable quality ($Q$) factors, field confinement, and overall sensitivity in surface-enhanced vibrational spectroscopy.

Recently, all-dielectric nanostructures, such as silicon, have attracted increasing interest[12] as promising alternatives, offering high polarizability, lower material absorption losses,[13] broad tunability of optical responses via collective resonances,[14,15] and compatibility with low-cost fabrication techniques. These advantages suggest that dielectric platforms could enable higher-performance infrared spectroscopy. Nevertheless, their SEIRA characteristics remain underexplored, with few studies investigating SEIRA based on all-dielectric nanostructures.[16−22] Quasi-bound states in the continuum (qBICs) in periodically arrayed nanostructures[23,24] have recently been shown to support vibrational coupling and enhance molecular signals;[18,21,25−27] however, a quantitative comparison between dielectric and plasmonic SEIRA platforms is lacking. One of the challenges in evaluating light−molecule interactions using qBICs is that the electromagnetic field distribution, resonance wavelength, and radiative losses vary with the degree of broken symmetry in the unit structures,[23,28] all of which influence the coupling efficiency between the qBICs and molecular vibrations. The coupling conditions also depend on the thickness of the surface-adsorbed molecular layers, as they

Received: August 28, 2025
Revised: November 10, 2025
Accepted: November 10, 2025
Published: November 17, 2025

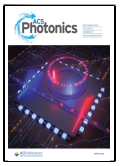

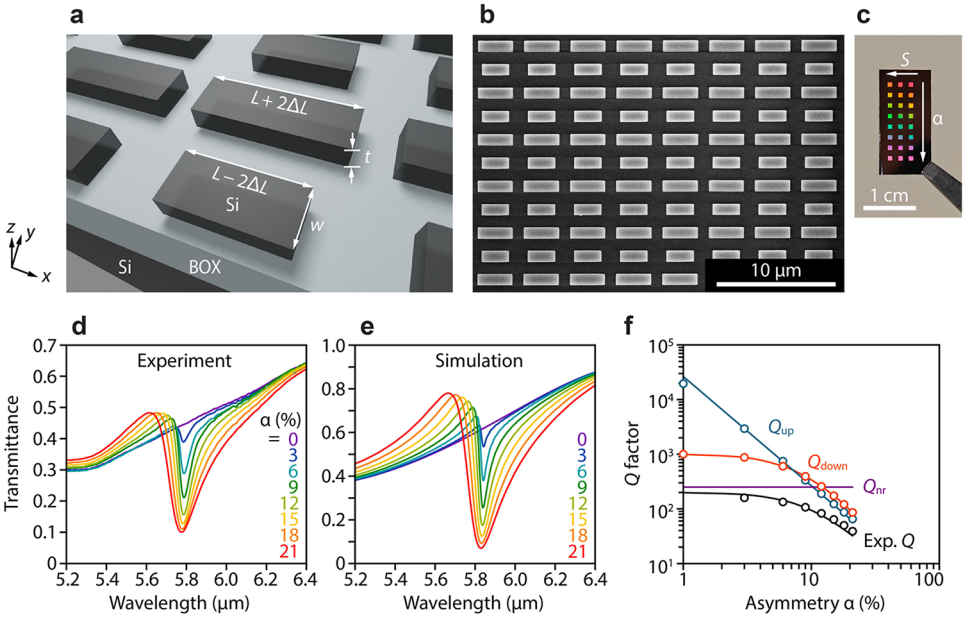


**Figure 1.** Silicon BIC metasurfaces ($S$ = 1.00) operating in the mid-infrared regime. (a) Schematic with key structural parameters. (b) SEM image of a fabricated metasurface with $\alpha$ = 12%. (c) Image of a fabricated device showing multiple metasurfaces with varied scaling factors $S$ and asymmetry parameter $\alpha$. (d) Measured and (e) simulated transmittance spectra for different $\alpha$. (f) Decomposed $Q$ factors along with a fitted curve (black) to the experimental $Q$ factors (black dots).

alter the spatial overlap between the electric field of qBICs and the vibrational modes of the molecules. Hence, a rigorous, systematic characterization of silicon BIC metasurfaces is essential to better understand and optimize the qBIC-based SEIRA.

In this study, we comprehensively characterize the SEIRA performance of silicon-based all-dielectric BIC metasurfaces and quantitatively assess their enhancement capabilities. We fabricated silicon BIC metasurfaces with varying geometric scaling factors and asymmetry parameters. Subsequently, the coupling with the C═O stretching mode of poly(methyl methacrylate) (PMMA) is investigated across different PMMA film thicknesses, radiative $Q$ factors, and resonance detuning. By modeling the spatial overlap between the electric field distribution of the qBIC and the PMMA layer, we estimate the number of molecules contributing to the enhanced molecular signal, yielding a SEIRA enhancement factor (EF) exceeding 1 × $10^4$, consistent with monolayer-level sensitivity.

## RESULTS AND DISCUSSION

**Basic Characteristics.** Silicon metasurfaces were fabricated by patterning nanostructures on the top silicon layer of commercial silicon-on-insulator (SOI) wafers, which comprised a 500 nm-thick top silicon layer and a 3000 nm-thick buried oxide (BOX) layer. Figure 1a shows a schematic of the metasurface design. The unit cell comprises two parallel silicon rods of different lengths arranged in a square lattice with a period of $P$ = 3900 nm, an initial rod length of $L$ = 2620 nm, and a width of $w$ = 920 nm. Modifying the lengths of the upper and lower rods to $L + \Delta L$ and $L - \Delta L$, respectively, breaks the symmetry of the system, thereby converting the symmetry-protected BIC into a quasi-BIC (qBIC) whose finite radiation components are accessible through free-space excitation. The fabrication was conducted by spin-coating a positive resist on the SOI wafers followed by electron beam lithography to define the nanopatterns. These written patterns were then transferred to the top silicon layer via deep reactive ion etching (BOSCH process) using $SF_6$ and $C_4H_8$ gases. Figure 1b,c shows a scanning electron microscopy (SEM) image of the fabricated metasurface and a photograph of the full device array. A total of 24 metasurfaces (800 $\mu$m × 800 $\mu$m) were fabricated with three different geometric scaling factors ($S$) and eight different asymmetry parameters ($\alpha$) defined as $\alpha = 2\Delta L/L$. In these designs, the period $P$ and silicon layer thickness were fixed, while the rod length $L$ and width $w$ were scaled by a factor of $S$. The transmittance spectra of the qBICs were measured by using Fourier transform infrared spectroscopy (FTIR) with a vertically incident $x$-polarized light source. Figure 1d,e shows a comparison of the measured and simulated transmittance spectra for BIC metasurfaces with varying $\alpha$ values. The results show good agreement, with the resonance peak wavelength remaining nearly constant across different $\alpha$. Moreover, an increase in the transmission dip depth and line width broadening was observed, consistent with the typical behavior of qBICs. The experimental $Q$ factors were extracted by fitting the spectra with a Fano resonance model (Figure S1), with the highest $Q$ factor reaching 175 at $\alpha$ = 3%. However, noticeable discrepancies between the experimental and simulated $Q$ factors were observed, particularly at small $\alpha$, as shown in Figure 1f. Here, the radiative $Q$ factor $Q_r$ was calculated using the relation $Q_r = \omega_0 U(t)/P(t)$,[29] where $\omega_0$ is the angular frequency of the resonance mode, $U(t)$ is the modal electromagnetic energy, and $P(t)$ is the radiation power through the computational domain boundaries. $P(t)$ can be further decomposed into upward and downward components, which, respectively, give the radiation $Q$ factors $Q_{up}$ and $Q_{down}$ that satisfy $Q_r^{-1} = Q_{up}^{-1} + Q_{down}^{-1}$. From Figure 1f, $Q_{up}$ follows the inverse square law of qBICs,[30] being proportional to $\alpha^{-2}$. In contrast, $Q_{down}$ deviates from this inverse square law, with $Q_{down} < Q_{up}$ at small $\alpha$. This behavior can be attributed to the asymmetric cladding layer of the SOI wafer, which causes additional radiation leakage into the buried oxide layer.[23,31]



https://doi.org/10.1021/acsphotonics.5c02042
ACS Photonics 2025, 12, 6876−6883

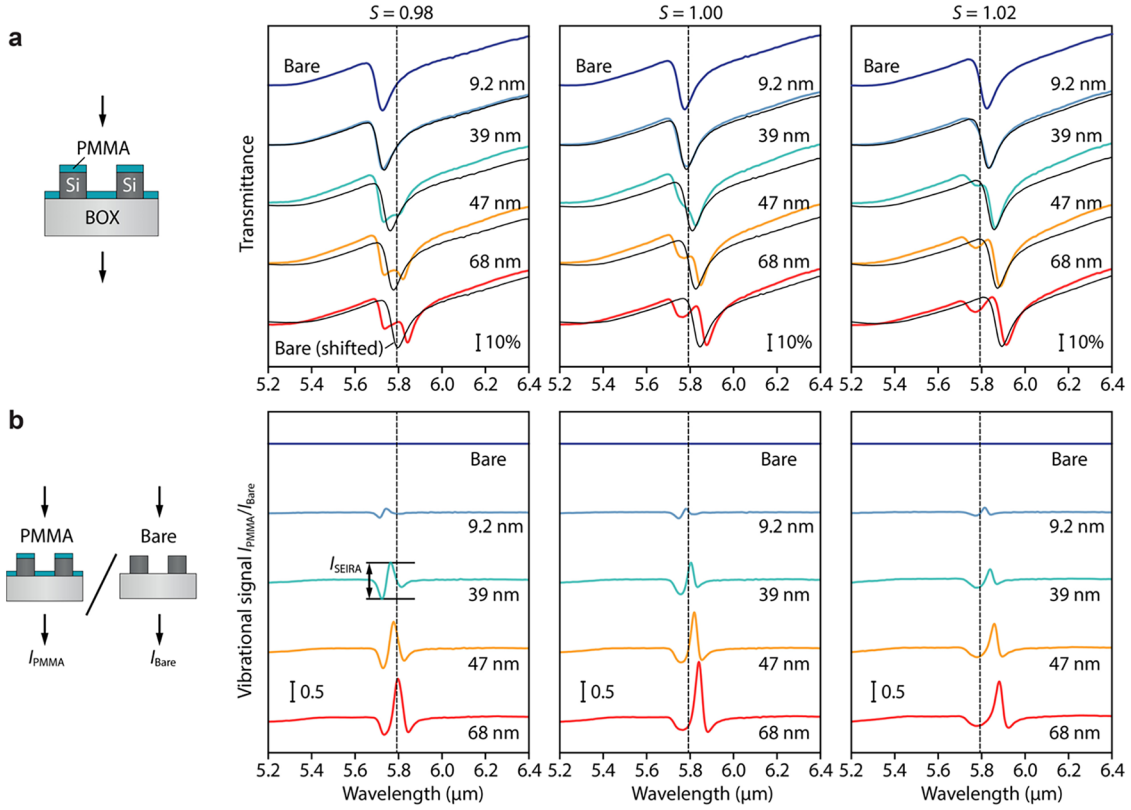


**Figure 2.** Coupling between PMMA molecules and qBICs of silicon metasurfaces with varying scaling factors $S$ = 0.98, 1.00, and 1.02. (a) Transmittance spectra for different PMMA film thicknesses. The black curves indicate the spectra of bare metasurfaces, corrected for the resonance red shift caused by PMMA binding. (b) Vibrational signal $I_{PMMA}/I_{bare}$ for different PMMA film thicknesses. Vertical dashed lines indicate the PMMA absorption peak. Spectra are vertically offset for clarity.

However, this downward leakage loss alone cannot fully explain the total $Q$ factor. To account for the discrepancy, we introduced nonradiative loss channels, where the total nonradiative loss can be expressed as $Q_{nr}^{-1} = Q_{abs}^{-1} + Q_{scat}^{-1}$, with $Q_{abs}^{-1}$ and $Q_{scat}^{-1}$ denoting material absorption and surface roughness-induced scattering losses, respectively. The total $Q$ factor was then successfully modeled by using $Q^{-1} = Q_{up}^{-1} + Q_{down}^{-1} + Q_{nr}^{-1}$, indicating that the nonradiative losses are the dominant limiting factor when $\alpha$ is smaller than approximately 10%. Note that the effect of materials absorption loss $Q_{abs}^{-1}$ in the BOX layer is negligibly small in the wavelength range of interest in this study (Supporting Information S2 for details).

**Vibrational Coupling.** PMMA films of varying thicknesses were spin-coated onto BIC metasurfaces to enable spatial and spectral coupling between the C═O stretching vibrational mode of PMMA and the qBICs. Figure 2a shows the measured transmittance spectra for metasurfaces with $\alpha$ = 12%. The resonance wavelength of the qBIC was tuned by varying the scaling factor, $S$, which controls the spectral detuning between the qBIC resonance and the PMMA absorption peak. With increasing thickness of the PMMA layer, substantial changes in the spectral features were observed near the PMMA absorption wavelength, including resonance peak shift and splitting. Since the resonance peak wavelength of the qBIC is itself affected by the thickness of the adsorbed PMMA film (Figure S3), the observed spectral changes in the coupled system reflect a combination of resonance red shift and amplitude modulation due to surface-enhanced infrared absorption. To isolate the vibrational enhancement from the red-shift effect, we first quantified the resonance shift induced by the PMMA adsorption using qBICs with large spectral detuning, where vibrational coupling is minimal. Based on this correction, we calculated the vibrational signal as the ratio $I_{PMMA}/I_{bare}$,[32] where $I_{PMMA}$ and $I_{bare}$ are the transmittances of the PMMA-coated and bare metasurfaces, respectively, with the red shift effect taken into account. As shown in Figure 2b, the vibrational signal increased with increasing PMMA thickness, consistent with stronger light−matter interactions for greater molecular vibrational bonds. Furthermore, the signal reached its maximum at $S$ = 1.00, corresponding to near-zero detuning between the qBIC resonance and the vibrational mode. Here, the small negative dips on either side of the vibrational signal peak can be attributed to spectral broadening and splitting of the transmittance spectra in PMMA-coated metasurfaces.

We next focused on the condition with a scaling factor of $S$ = 1.00 and further investigated the SEIRA characteristics in detail. Figure 3a presents the enhanced molecular signal, which is defined as the peak-to-peak amplitude of the vibrational signal $I_{PMMA}/I_{bare}$, as a function of asymmetry parameter $\alpha$ for various PMMA film thicknesses. In all the cases, the enhanced molecular signal increased with $\alpha$ and saturated at approximately $\alpha$ = 12%. Figure 3b shows the experimental transmittance spectra and corresponding vibrational signals for a PMMA thickness of $t_{PMMA}$ = 47 nm. As $\alpha$ increased, the transmittance dip deepened, while the vibrational signal peaked at $\alpha$ = 15%. Although higher $Q$ factors and stronger field enhancement at smaller $\alpha$ are generally expected to yield greater signal enhancement, the experimental results showed the opposite trend (i.e., larger vibrational signals were observed


https://doi.org/10.1021/acsphotonics.5c02042
ACS Photonics 2025, 12, 6876−6883

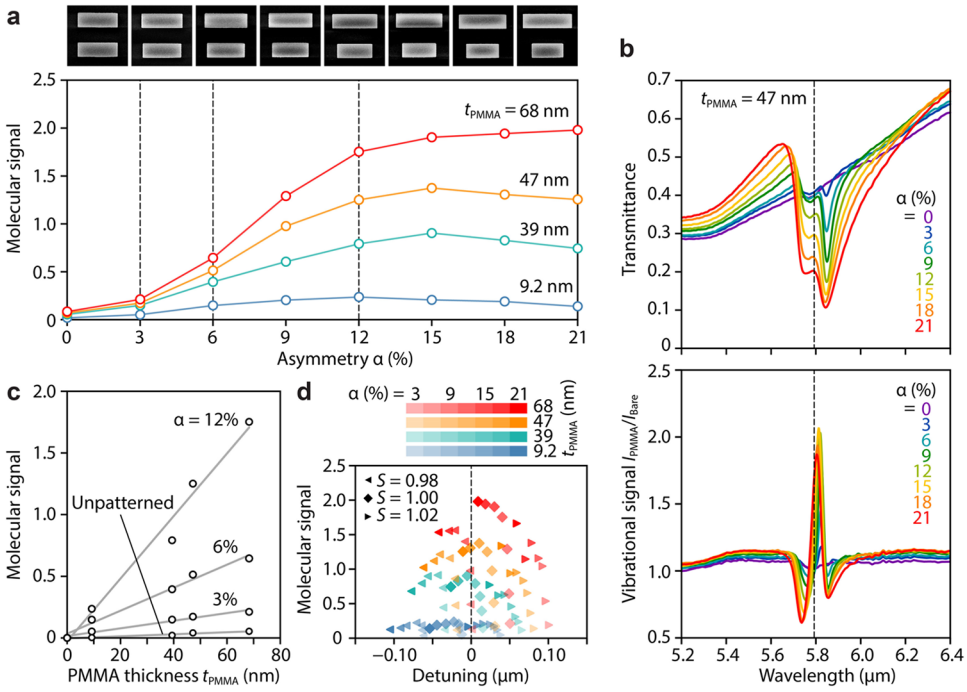


**Figure 3.** Comprehensive characterization of the enhanced molecular signal for metasurfaces with a scaling factor $S$ = 1.00. (a) Enhanced molecular signals for various PMMA film thicknesses $t_{PMMA}$ plotted against asymmetry parameter $\alpha$. The inset shows the SEM images of the unit structures at different $\alpha$. (b) Transmittance spectra (top) and corresponding vibrational signals (bottom) for different $\alpha$ at $t_{PMMA}$ = 47 nm. (c) Thickness dependence of the enhanced molecular signal for $\alpha$ = 3, 6, and 12%, and for an unpatterned control sample. (d) Scatter plot of the enhanced molecular signal versus detuning for various PMMA thicknesses $t_{PMMA}$, scaling factors $S$, and asymmetry parameters $\alpha$.

at larger $\alpha$). This behavior can be explained by the fact that the radiation loss varies with $\alpha$, which directly influences the interaction between the qBICs and surface-adsorbed molecules. When $\alpha$ is small, the high radiative $Q$ factor confines the resonantly enhanced electromagnetic field predominantly inside the silicon, limiting its interaction with the external molecules. Conversely, as $\alpha$ increases, the qBIC becomes more radiative, enhancing its interaction with the molecular overlayer. However, the decreasing radiative $Q$ factor and hence the decreasing field intensity limit further enhancement beyond a certain $\alpha$, resulting in signal saturation. More precisely, the strength of the vibrational signal depends on the complex interplay between the radiative and nonradiative $Q$ factors of the qBICs, their coupling strength with molecular vibrations, and spectral detuning. These dependencies can be analytically captured by the temporal coupled mode theory.[23,33] Figure 3c shows the enhanced molecular signal as a function of the PMMA film thickness for several $\alpha$ and a comparison of the signal with that of an unpatterned control sample. All the conditions exhibited a linear dependence on the PMMA thickness. The unpatterned sample, fabricated by removing the top silicon layer from the SOI wafer and depositing PMMA films of different thickness, also displayed a linear response. Notably, the enhanced molecular signal in the BIC metasurface with $\alpha$ = 12% was approximately 70 times greater than that of the unpatterned sample at a PMMA thickness of 9.2 nm (Figure S4 for the spectra of the unpatterned sample). Finally, Figure 3d plots the enhanced molecular signal as a function of detuning, defined as the difference between the resonance center wavelength of the qBIC (determined by Fano fitting) and the absorption peak of PMMA (determined by spectroscopic ellipsometry; see Supporting Information S5). The scatter plot, comprising data points from various $t_{PMMA}$, $S$, and $\alpha$, shows that the molecular signal was maximum at near-zero detuning, in agreement with theoretical expectations. Although this scatter plot involves multiple parameters, which complicates its interpretation, focusing solely on the $\alpha$ values that yield the largest signal for each film thickness leads to the same conclusion: as detuning approaches zero, the signal strength increases and reaches the maximum.

**SEIRA Enhancement Factor.** We characterized the SEIRA performance of silicon metasurfaces coated with thin PMMA films. Figure 4a shows the transmittance spectra for $\alpha$ = 12%. For all values of scaling factor $S$, we observed a distinct shift in the resonance wavelength and a change in the transmittance depending on the PMMA thickness. Even for PMMA films only several nanometers thick, a clear enhanced molecular signal was observed. From a microscopic perspective, this enhanced molecular signal can be attributed to the spatial overlap between the surface-adsorbed PMMA molecules and the electric field of the qBICs. Since the strength of light–matter interaction strongly depends on the out-of-plane distribution of the molecules, the PMMA thickness plays a crucial role in modulating the SEIRA response. To further explore this, we calculated the cross-sectional distribution of the maximum electric field enhancement $|E|^2$ in the $xy$-plane at various $z$-positions, as shown in Figure 4b. The strongest enhancement appears at the interface between the BOX layer and the bottom of the silicon nanorods ($z$ = −250 nm), where the electric field is localized at both ends of the paired rods. Similarly, strong electric field enhancement is observed at the top surface of the nanorods ($z$ = 250 nm) due to the high refractive index contrast between silicon and air. Importantly, spin-coated PMMA films cover both the top and bottom interfaces ($z$ = ±250 nm), allowing the molecules to strongly


https://doi.org/10.1021/acsphotonics.5c02042
ACS Photonics 2025, 12, 6876−6883

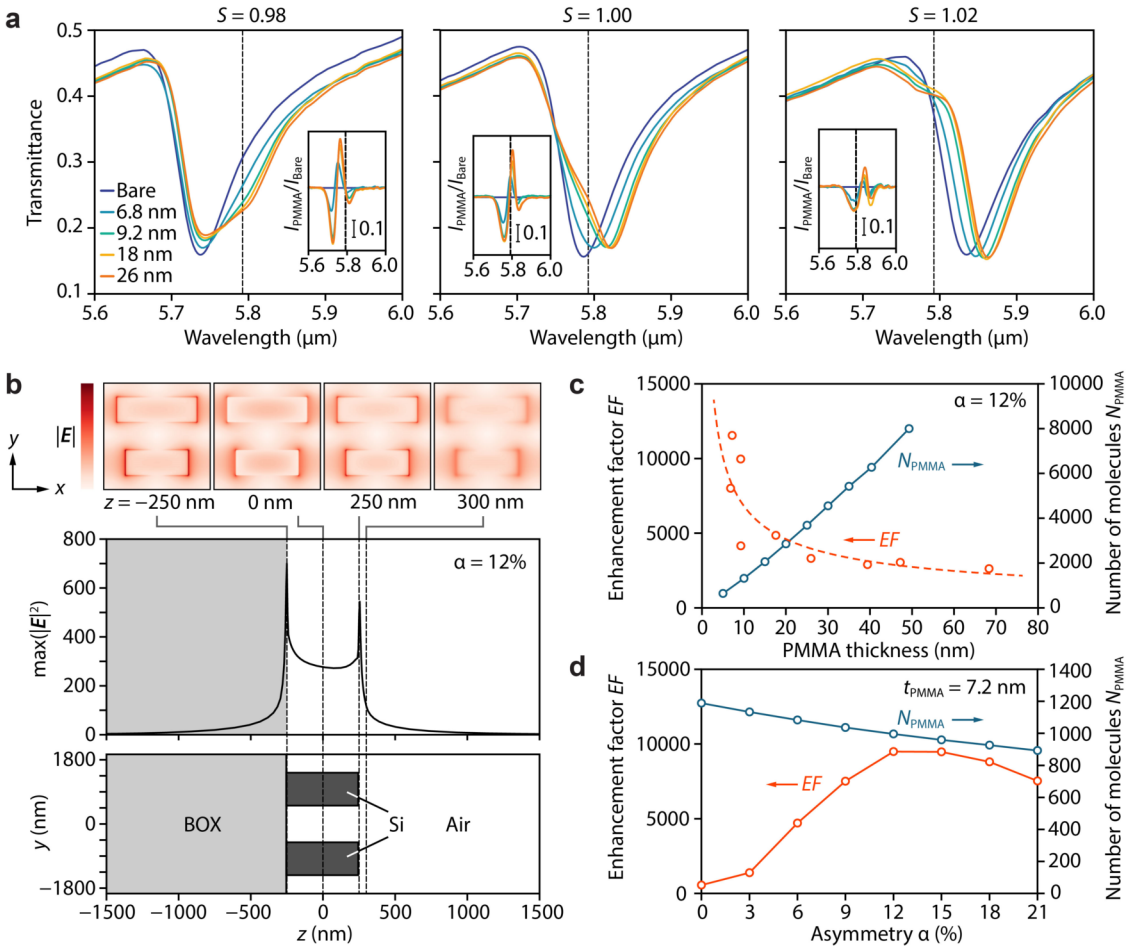


**Figure 4.** Characterization of the SEIRA performance of silicon BIC metasurfaces using thin PMMA films. (a) Transmittance spectra for different PMMA film thicknesses. The spectra are compared with different scaling factors, $S$ = 0.98, 1.00, and 1.02, from left to right. Vertical dashed lines indicate PMMA absorption peak wavelengths. Insets show the corresponding vibrational signals. (b) Electric field enhancement effect in the $z$-direction for $\alpha$ = 12%. Color maps of the electric field $|\boldsymbol{E}|$ in the $xy$-plane at selected $z$-positions (top), plot of the maximum $|\boldsymbol{E}|^2$ versus $z$ (middle), and corresponding metasurface structure (bottom, not to scale in the vertical direction). (c) SEIRA enhancement factor EF and number of PMMA molecules $N_{\mathrm{PMMA}}$ per unit cell as a function of PMMA film thickness $t_{\mathrm{PMMA}}$ for $\alpha$ = 12%. The red dashed curve is the fitted trend of the EF. (d) EF and $N_{\mathrm{PMMA}}$ per unit cell as a function of $\alpha$ when $t_{\mathrm{PMMA}}$ is 7.2 nm.

interact with the highly localized electric fields of the qBICs. By considering the overlap integral between the electric field $E(\mathbf{r})$ and the spatial distribution of the PMMA layer, we can quantitatively estimate the number of molecules that contribute to the enhanced molecular signal using the following equation[34,35]

$$N_{\mathrm{PMMA}} = \frac{\int_{\mathrm{PMMA}} \varepsilon |E(\mathbf{r})|^2 \mathrm{d}V}{\max[\varepsilon(\mathbf{r})|E(\mathbf{r})|^2]} \cdot \frac{\rho N_{\mathrm{A}}}{M} \tag{1}$$

where $\varepsilon(\mathbf{r})$ is the permittivity of the given material, $\rho$ is the density of PMMA molecules, $N_{\mathrm{A}}$ is the Avogadro constant, and $M$ is the molecular weight of PMMA molecules. Using the calculated $N_{\mathrm{PMMA}}$, we can evaluate the SEIRA enhancement factor (EF), defined as follows[36]

$$\mathrm{EF} = \frac{I_{\mathrm{SEIRA}}}{I_{\mathrm{unpatterned}}} \cdot \frac{N_{\mathrm{unpatterned}}}{N_{\mathrm{PMMA}}} \tag{2}$$

where $I_{\mathrm{SEIRA}}$ and $I_{\mathrm{unpatterned}}$ represent the enhanced molecular signals from the metasurface with and without nanostructures, respectively, and $N_{\mathrm{PMMA}}$ and $N_{\mathrm{unpatterned}}$ are the numbers of molecules contributing to the molecular signal in each case.

Figure 4c shows the calculated values of $N_{\mathrm{PMMA}}$ per unit cell and the corresponding SEIRA enhancement factors for $\alpha$ = 12%. As expected, $N_{\mathrm{PMMA}}$ decreases with decreasing PMMA film thickness. At the same time, EF exhibited a marked increase for thinner PMMA films. Notably, the maximum EF was found to be EF = $1.2 \times 10^4$ at a PMMA thickness of 7.2 nm. In this case, the number of molecules contributing to the enhanced molecular signal can be estimated to be approximately 1000 per unit cell, corresponding to zeptomole-level detection sensitivity. Note that 1000 PMMA molecules correspond to approximately $10^7$ C═O bonds, because the number of C═O bonds in a PMMA molecule with a molecular weight of 950 kDa can be calculated to be approximately 9490 for a monomer methyl methacrylate weight of 100.12 g/mol. Figure 4d shows the dependence of both $N_{\mathrm{PMMA}}$ and EF on $\alpha$, with the PMMA thickness fixed at 7.2 nm. While $N_{\mathrm{PMMA}}$ gradually decreased with increasing $\alpha$, EF varied more significantly and reached its maximum at $\alpha$ = 12%, consistent with the maximum vibrational signal observed in Figure 3a. Comparing our results with the values reported (see also Supporting Information Table S1) for plasmonic nanostructures, such as gold cross nanoantennas[37] with EF =


https://doi.org/10.1021/acsphotonics.5c02042
ACS Photonics 2025, 12, 6876−6883

$1.2 \times 10^4$, nanoporous gold disks[38] with EF = $2.3 \times 10^4$, and gold multilayer metafilms[39] with EF = $8.3 \times 10^3$, all of which were used for detecting self-assembled monolayers, we find that our silicon metasurfaces achieved a comparable EF. This indicates that all-dielectric metasurfaces can provide monolayer-level sensitivity, highlighting their potential as promising platforms for SEIRA spectroscopy. To the best of our knowledge, our study is the first to accurately estimate the EF of all-dielectric nanostructures, for which only a few SEIRA studies have been reported, with the EF evaluated to date being 13.3 using silicon photonic crystals.[19] It should be noted that the EF of SEIRA can be enhanced by one to 2 orders of magnitude when nanogaps of several nanometers, where electromagnetic fields are strongly localized and enhanced, are introduced.[32,40] The same principle should apply to all-dielectric metasurfaces, and a similar enhancement can be expected by introducing nanogaps in the middle of silicon paired nanorods.[41] Given that the high EF arises from the strong electric field enhancement, the potential applications of our silicon metasurfaces are not limited to SEIRA but can also be extended to nonlinear spectroscopies such as Raman,[42,43] two-dimensional infrared,[44] and higher-order infrared spectroscopies,[45] where the enhancement factors scale with the fourth or even sixth power of the electric field.

## CONCLUSIONS

In this study, we systematically characterized the SEIRA performance of silicon BIC metasurfaces composed of paired nanorods and demonstrated their capability for highly sensitive infrared spectroscopy. By spin-coating a few nanometers of PMMA films onto the metasurfaces, we achieved spectral coupling between the C═O stretching vibrational modes of PMMA molecules and the qBICs. The enhanced molecular vibrational signal exhibited a clear linear dependence on the PMMA film thickness. Furthermore, we found that the enhanced molecular signal reached a maximum at a specific the asymmetry parameter of the BIC metasurface and under near-zero detuning conditions. To quantitatively evaluate the SEIRA enhancement factors, we estimated the number of molecules contributing to the signal enhancement by calculating the overlap integral between the localized electric fields and the surface-adsorbed PMMA layers. Consequently, we found that the enhancement factor reached as high as $10^4$ when the PMMA film was sufficiently thin, corresponding to monolayer-level sensitivity. These findings confirm that all-dielectric nanostructures can serve as a noble metal-free yet highly effective platform for surface-enhanced infrared spectroscopy. Our work offers new opportunities for label-free molecular sensing at low concentrations and also complements the drawbacks of conventional metal-based SERS and SEIRA techniques.

## METHODS

**Fabrication.** Prior to fabrication, SOI wafers with a 500 nm-thick top silicon layer and a 3000 nm-thick BOX layer were cleaned with acetone and isopropyl alcohol (IPA) in an ultrasonic bath, followed by oxygen plasma treatment. A 100 nm-thick layer of a positive electron beam resist (ZEP520A, Zeon Chemicals) was spin-coated onto the top silicon surface and prebaked on a hot plate at 180 °C for 3 min. Subsequently, a conductive layer (ESPACER 300Z, Showa Denko) was spin-coated at 2000 rpm for 60 s. The metasurface patterns were written using electron beam lithography (ELS-BODEN, Elionix) at an area dose of 220 $\mu C/cm^2$ and an acceleration voltage of 100 kV. After exposure, the resist was developed in xylene for 60 s and rinsed with IPA for 30 s. The developed patterns were transferred into the top silicon layer using silicon deep reactive ion etching equipment (MUC-21 ASE-SRE, Sumitomo Precision Products) with $SF_6$ and $C_4H_8$ as the etching and passivation gases, respectively. Finally, the residual resist was removed by using the water vapor plasma treatment (AQ-500, Samco).

**Characterization.** Transmittance spectra of the fabricated metasurfaces were measured by using a Fourier transform infrared spectrometer (Nicolet iS50R, Thermo Fisher Scientific). Measurements were performed with a custom-built transmission optical setup inside the sample compartment, allowing automated positioning of the metasurfaces with multiple structural parameters by using a motorized stage for stable and reproducible data acquisition. The qBICs were excited under normal incidence with $x$-polarized light focused through an iris diaphragm (0.7 mm in diameter), and the transmitted light was collected by a liquid nitrogen-cooled mercury cadmium telluride detector with a spectral resolution of 4 $cm^{-1}$. The sample compartment was purged with nitrogen gas to suppress unwanted atmospheric absorption. For coupling experiments with PMMA molecules, diluted PMMA solutions (950 kDa) were spin-coated onto the metasurfaces and baked at 180 °C for 90 s on a hot plate. The PMMA film thicknesses were determined by using a spectroscopic ellipsometer (M-2000, J.A. Woollam).

**Simulation.** Transmittance spectra and electric field distributions were simulated by using a commercial finite-difference time-domain (FDTD) solver (Ansys Lumerical). Perfectly matched layer boundary conditions were applied along the $z$-axis, while Bloch boundary conditions were employed along the $x$ and $y$ axes. The radiative $Q$ factor $Q_r$ was calculated as $Q_r = \omega_0 U(t)/P(t)$, where $\omega_0$ is the resonant frequency, $U(t)$ is the electromagnetic energy stored in the mode, and $P(t)$ is the radiation power absorbed through the simulation boundaries. Directional $Q$ factors $Q_{up}$ and $Q_{down}$ were calculated by separating $P(t)$ into upward $P_{up}(t)$ and downward $P_{down}(t)$ components, whose boundaries are positioned approximately at $\lambda/4$ above and below the silicon surface, respectively. Since the Bloch boundary conditions are used in the $x$ and $y$ directions, radiation in the in-plane direction was assumed to be zero. In all $Q$ factor calculations, the refractive index $n$ was set to 3.425 for silicon and 1.290 for $SiO_2$, with their extinction coefficient $k$ being zero. To estimate the number of PMMA molecules contributing to the SEIRA signal per unit cell, the spatial overlap between the modal electric fields and the PMMA layer (assumed to have zero $k$) was considered. PMMA layers were assumed to be adsorbed on both the BOX and the top surfaces of the silicon nanostructures, while no adsorption on the sidewalls was assumed owing to the use of a fast spin-coating process that limits polymer infiltration into the vertical features.

## ASSOCIATED CONTENT

### Supporting Information

The Supporting Information is available free of charge at https://pubs.acs.org/doi/10.1021/acsphotonics.5c02042.

Fano fitting; $Q$ factors considering $SiO_2$ material absorption; relationship between enhanced molecular



https://doi.org/10.1021/acsphotonics.5c02042
ACS Photonics 2025, 12, 6876−6883

vibrational signal and wavelength shift; enhanced molecular vibrational signal from unpatterned substrates; optical constants of PMMA; comparison of SEIRA performance (PDF)

## AUTHOR INFORMATION


### Corresponding Author

**Keisuke Watanabe** − *International Center for Materials Nanoarchitectonics (MANA), National Institute for Materials Science (NIMS), Tsukuba, Ibaraki 305-0044, Japan;* orcid.org/0000-0002-4285-2135; Email: watanabe.keisuke@nims.go.jp

### Author

**Tadaaki Nagao** − *International Center for Materials Nanoarchitectonics (MANA), National Institute for Materials Science (NIMS), Tsukuba, Ibaraki 305-0044, Japan; Department of Condensed Matter Physics, Graduate School of Science, Hokkaido University, Sapporo 060-0810, Japan;* orcid.org/0000-0002-6746-2686

Complete contact information is available at: https://pubs.acs.org/10.1021/acsphotonics.5c02042


### Author Contributions

K.W. conceived the idea, performed most of the experiments and simulations, analyzed the data, and drafted the manuscript. T.N. supervised the project and discussed the results. The manuscript was written through contributions of all authors. All authors have given approval to the final version of the manuscript.


### Funding

This work was financially supported by JSPS KAKENHI (JP22K20496 and JP24K17583).


### Notes

The authors declare no competing financial interest.


## ACKNOWLEDGMENTS

The authors acknowledge support from "Advanced Research Infrastructure for Materials and Nanotechnology in Japan (ARIM)" of the Ministry of Education, Culture, Sports, Science and Technology (MEXT), Japan (JPMXP1223NM5060, JPMXP1224NM5259).


## REFERENCES


(1) Altug, H.; Oh, S. H.; Maier, S. A.; Homola, J. Advances and Applications of Nanophotonic Biosensors. *Nat. Nanotechnol.* **2022**, *17*, 5−16.

(2) López-Lorente, Á. I.; Mizaikoff, B. Mid-Infrared Spectroscopy for Protein Analysis: Potential and Challenges. *Anal. Bioanal. Chem.* **2016**, *408* (11), 2875−2889.

(3) Kozuch, J.; Ataka, K.; Heberle, J. Surface-Enhanced Infrared Absorption Spectroscopy. *Nat. Rev. Methods Primers* **2023**, *3* (1), No. 70.

(4) Wang, X.; Huang, S. C.; Hu, S.; Yan, S.; Ren, B. Fundamental Understanding and Applications of Plasmon-Enhanced Raman Spectroscopy. *Nat. Rev. Phys.* **2020**, *2* (5), 253−271.

(5) Adato, R.; Aksu, S.; Altug, H. Engineering Mid-Infrared Nanoantennas for Surface Enhanced Infrared Absorption Spectroscopy. *Mater. Today* **2015**, *18* (8), 436−446, DOI: 10.1016/j.mattod.2015.03.001.

(6) Li, D.; Wu, X.; Chen, Z.; Liu, T.; Mu, X. Surface-Enhanced Spectroscopy Technology Based on Metamaterials. *Microsyst. Nanoeng.* **2025**, *11* (1), No. 60.

(7) Enders, D.; Nagao, T.; Nakayama, T.; Aono, M. In Situ Surface-Enhanced Infrared Absorption Spectroscopy for the Analysis of the Adsorption and Desorption Process of Au Nanoparticles on the SiO2/Si Surface. *Langmuir* **2007**, *23* (11), 6119−6125.

(8) Neubrech, F.; Pucci, A.; Cornelius, T. W.; Karim, S.; García-Etxarri, A.; Aizpurua, J. Resonant Plasmonic and Vibrational Coupling in a Tailored Nanoantenna for Infrared Detection. *Phys. Rev. Lett.* **2008**, *101* (15), No. 157403.

(9) Nigorinuma, H.; Nishijima, Y.; Juodkazis, S.; Rosa, L. Selective Enhancement of Infrared Absorption with Metal Hole Arrays. *Opt. Mater. Express* **2012**, *2* (10), 1367−1377.

(10) Chen, K.; Dao, T. D.; Ishii, S.; Aono, M.; Nagao, T. Infrared Aluminum Metamaterial Perfect Absorbers for Plasmon-Enhanced Infrared Spectroscopy. *Adv. Funct. Mater.* **2015**, *25* (42), 6637−6643.

(11) Paggi, L.; Fabas, A.; El Ouazzani, H.; Hugonin, J. P.; Fayard, N.; Bardou, N.; Dupuis, C.; Greffet, J. J.; Bouchon, P. Over-Coupled Resonator for Broadband Surface Enhanced Infrared Absorption (SEIRA). *Nat. Commun.* **2023**, *14* (1), No. 4814.

(12) Jahani, S.; Jacob, Z. All-Dielectric Metamaterials. *Nat. Nanotechnol.* **2016**, *11* (1), 23−36, DOI: 10.1038/nnano.2015.304.

(13) Albella, P.; Poyli, M. A.; Schmidt, M. K.; Maier, S. A.; Moreno, F.; Sáenz, J. J.; Aizpurua, J. Low-Loss Electric and Magnetic Field-Enhanced Spectroscopy with Subwavelength Silicon Dimers. *J. Phys. Chem. C* **2013**, *117* (26), 13573−13584.

(14) Li, J.; Verellen, N.; Van Dorpe, P. Engineering Electric and Magnetic Dipole Coupling in Arrays of Dielectric Nanoparticles. *J. Appl. Phys.* **2018**, *123* (8), No. 083101.

(15) Koshelev, K.; Favraud, G.; Bogdanov, A.; Kivshar, Y.; Fratalocchi, A. Nonradiating Photonics with Resonant Dielectric Nanostructures. *Nanophotonics* **2019**, *8* (5), 725−745.

(16) Nitkowski, A.; Chen, L.; Lipson, M. Cavity-Enhanced on-Chip Absorption Spectroscopy Using Microring Resonators. *Opt. Express* **2008**, *16* (16), 11930.

(17) Chen, Y.; Lin, H.; Hu, J.; Li, M. Heterogeneously Integrated Silicon Photonics for the Mid-Infrared and Spectroscopic Sensing. *ACS Nano* **2014**, *8* (7), 6955−6961.

(18) Tittl, A.; Leitis, A.; Liu, M.; Yesilkoy, F.; Choi, D. Y.; Neshev, D. N.; Kivshar, Y. S.; Altug, H. Imaging-Based Molecular Barcoding with Pixelated Dielectric Metasurfaces. *Science* **2018**, *360* (6393), 1105−1109.

(19) Chang, Y.; Hasan, D.; Dong, B.; Wei, J.; Ma, Y.; Zhou, G.; Ang, K. W.; Lee, C. All-Dielectric Surface-Enhanced Infrared Absorption-Based Gas Sensor Using Guided Resonance. *ACS Appl. Mater. Interfaces* **2018**, *10* (44), 38272−38279.

(20) Kharratian, S.; Conteduca, D.; Procacci, B.; Shaw, D. J.; Hunt, N. T.; Krauss, T. F. Metasurface-Enhanced Mid-Infrared Spectroscopy in the Liquid Phase. *Chem. Sci.* **2022**, *13* (43), 12858−12864.

(21) Chong, H.; Zhang, W.; Mu, Y.; Ye, H.; Cai, Y. Ultra-Narrowband Dielectric Metasurfaces for Surface-Enhanced Infrared Absorption. *Appl. Phys. Lett.* **2025**, *126* (9), No. 091701, DOI: 10.1063/5.0255749.

(22) Wei, Y.; Si, L.; Han, K.; Xu, H.; Bao, X.; Zhu, W. Quasi-BIC-Enhanced Integrated Sensing Dielectric Metasurfaces for Molecular Fingerprint Retrieval and Chiral Detection. *Nanoscale* **2025**, *17* (13), 8005−8015.

(23) Watanabe, K.; Devi, H. R.; Iwanaga, M.; Nagao, T. Vibrational Coupling to Quasi-Bound States in the Continuum under Tailored Coupling Conditions. *Adv. Opt. Mater.* **2024**, *12* (6), No. 2301912.

(24) Adi, W.; Rosas, S.; Beisenova, A.; Biswas, S. K.; Mei, H.; Czaplewski, D. A.; Yesilkoy, F. Trapping Light in Air with Membrane Metasurfaces for Vibrational Strong Coupling. *Nat. Commun.* **2024**, *15* (1), No. 10049.

(25) Aigner, A.; Tittl, A.; Wang, J.; Weber, T.; Kivshar, Y.; Maier, S. A.; Ren, H. Plasmonic Bound States in the Continuum to Tailor Light-Matter Coupling. *Sci. Adv.* **2022**, *8* (49), No. eadd4816, DOI: 10.1126/sciadv.add4816.

(26) Wang, J.; Weber, T.; Aigner, A.; Maier, S. A.; Tittl, A.; Wang, J.; Weber, T.; Aigner, A.; Maier, S. A.; Tittl, A. Mirror-Coupled

Plasmonic Bound States in the Continuum for Tunable Perfect Absorption. *Laser Photonics Rev.* **2023**, *17*, No. 2300294.
(27) Aigner, A.; Weber, T.; Wester, A.; Maier, S. A.; Tittl, A. Continuous Spectral and Coupling-Strength Encoding with Dual-Gradient Metasurfaces. *Nat. Nanotechnol.* **2024**, *19*, 1804−1812.
(28) Weber, T.; Kühner, L.; Sortino, L.; Ben Mhenni, A.; Wilson, N. P.; Kühne, J.; Finley, J. J.; Maier, S. A.; Tittl, A. Intrinsic Strong Light-Matter Coupling with Self-Hybridized Bound States in the Continuum in van Der Waals Metasurfaces. *Nat. Mater.* **2023**, *22* (8), 970−976.
(29) Srinivasan, K.; Painter, O. Momentum Space Design of High-Q Photonic Crystal Optical Cavities. *Opt. Express* **2002**, *10* (15), 670−684.
(30) Koshelev, K.; Lepeshov, S.; Liu, M.; Bogdanov, A.; Kivshar, Y. Asymmetric Metasurfaces with High- Q Resonances Governed by Bound States in the Continuum. *Phys. Rev. Lett.* **2018**, *121* (19), No. 193903.
(31) Sadrieva, Z. F.; Sinev, I. S.; Koshelev, K. L.; Samusev, A.; Iorsh, I. V.; Takayama, O.; Malureanu, R.; Bogdanov, A. A.; Lavrinenko, A. V. Transition from Optical Bound States in the Continuum to Leaky Resonances: Role of Substrate and Roughness. *ACS Photonics* **2017**, *4* (4), 723−727.
(32) Huck, C.; Neubrech, F.; Vogt, J.; Toma, A.; Gerbert, D.; Katzmann, J.; Härtling, T.; Pucci, A. Surface-Enhanced Infrared Spectroscopy Using Nanometer-Sized Gaps. *ACS Nano* **2014**, *8* (5), 4908−4914.
(33) Agrawal, A.; Singh, A.; Yazdi, S.; Singh, A.; Ong, G. K.; Bustillo, K.; Johns, R. W.; Ringe, E.; Milliron, D. J. Resonant Coupling between Molecular Vibrations and Localized Surface Plasmon Resonance of Faceted Metal Oxide Nanocrystals. *Nano Lett.* **2017**, *17* (4), 2611−2620.
(34) Shalabney, A.; George, J.; Hutchison, J.; Pupillo, G.; Genet, C.; Ebbesen, T. W. Coherent Coupling of Molecular Resonators with a Microcavity Mode. *Nat. Commun.* **2015**, *6* (1), No. 5981.
(35) Koshelev, K. L.; Sychev, S. K.; Sadrieva, Z. F.; Bogdanov, A. A.; Iorsh, I. V. Strong Coupling between Excitons in Transition Metal Dichalcogenides and Optical Bound States in the Continuum. *Phys. Rev. B* **2018**, *98* (16), No. 161113.
(36) Dao, T. D.; Chen, K.; Nagao, T. Dual-Band in Situ Molecular Spectroscopy Using Single-Sized Al-Disk Perfect Absorbers. *Nanoscale* **2019**, *11* (19), 9508−9517.
(37) Brown, L. V.; Zhao, K.; King, N.; Sobhani, H.; Nordlander, P.; Halas, N. J. Surface-Enhanced Infrared Absorption Using Individual Cross Antennas Tailored to Chemical Moieties. *J. Am. Chem. Soc.* **2013**, *135* (9), 3688−3695.
(38) Shih, W. C.; Santos, G. M.; Zhao, F.; Zenasni, O.; Arnob, M. M. P. Simultaneous Chemical and Refractive Index Sensing in the 1−2.5 Mm near-Infrared Wavelength Range on Nanoporous Gold Disks. *Nano Lett.* **2016**, *16* (7), 4641−4647.
(39) Arul, R.; Grys, D. B.; Chikkaraddy, R.; Mueller, N. S.; Xomalis, A.; Miele, E.; Euser, T. G.; Baumberg, J. J. Giant Mid-IR Resonant Coupling to Molecular Vibrations in Sub-Nm Gaps of Plasmonic Multilayer Metafilms. *Light: Sci. Appl.* **2022**, *11* (1), No. 281.
(40) Dong, L.; Yang, X.; Zhang, C.; Cerjan, B.; Zhou, L.; Tseng, M. L.; Zhang, Y.; Alabastri, A.; Nordlander, P.; Halas, N. J. Nanogapped Au Antennas for Ultrasensitive Surface-Enhanced Infrared Absorption Spectroscopy. *Nano Lett.* **2017**, *17* (9), 5768−5774.
(41) Zhang, J.; Liu, W.; Zhu, Z.; Yuan, X.; Qin, S. Strong Field Enhancement and Light-Matter Interactions with All-Dielectric Metamaterials Based on Split Bar Resonators. *Opt. Express* **2014**, *22* (25), 30889.
(42) Wi, J.-S.; Tominaka, S.; Uosaki, K.; Nagao, T. Porous Gold Nanodisks with Multiple Internal Hot Spots. *Phys. Chem. Chem. Phys.* **2012**, *14* (25), 9131−9136.
(43) Hu, H.; Pal, A. K.; Berestennikov, A.; Weber, T.; Stefancu, A.; Cortés, E.; Maier, S. A.; Tittl, A. Surface-Enhanced Raman Scattering in BIC-Driven Semiconductor Metasurfaces. *Adv. Opt. Mater.* **2024**, *12* (14), No. 2302812.
(44) Noda, I. Two-Dimensional Infrared Spectroscopy. *J. Am. Chem. Soc.* **1989**, *111* (21), 8116−8118.
(45) MacKin, R. T.; Cohn, B.; Chuntonov, L.; Rubtsov, I. V. Intense-Field Interaction Regime with Weak Laser Pulses and Localized Plasmonic Enhancement: Reference-Free Demonstration by 3rd- and 5th-Order Infrared Spectroscopies. *J. Chem. Phys.* **2019**, *151* (12), No. 121103.




https://doi.org/10.1021/acsphotonics.5c02042
*ACS Photonics* 2025, 12, 6876−6883